PERIODICO di MINERALOGIA
established in 1930

Dipartimento
di Scienze della Terra
Sapienza
Università di Roma

An International Journal of
Mineralogy, Crystallography, Geochemistry,
Ore Deposits, Petrology, Volcanology
and applied topics on Environment, Archaeometry and Cultural Heritage

Geochemical and fluid inclusion studies on gold-bearing quartz veins and the host andesitic rocks in the Miardan gold deposit, NW Iran

Fatemeh Jahangiryar [1,*], Samad Alipour [2], Vartan Simmonds [3], Alexander Tvalchrelidzeh [4]

[1] Ph.D. in Economic Geology, Geology Department, Faculty of Sciences, Urmia University, Urmia, Iran
[2] Professor of Geochemistry, Geology Department, Faculty of Sciences, Urmia University, Urmia, Iran
[3] Associate professor of Economic Geology, Geosciences Department, Faculty of Natural Sciences, University of Tabriz, Tabriz, Iran
[4] Professor of Economic Geology, Senior Consultant of Zarjouian Company, Tabriz, Iran

ARTICLE INFO

Submitted: July 2020
Accepted: March 2022
Available on line: March 2022

* Corresponding author:
fjahangiryar@yahoo.com

Doi: 10.13133/2239-1002/16875

How to cite this article:
Jahangiryar F. et al. (2022)
Period. Mineral. 91, 89-111

ABSTRACT

The Miardan gold deposit in northwest Iran is located 15 km west of the Bostanabad town. The main rock units in the area include Eocene andesitic and trachy-andesitic rocks, along with tuff and ignimbrite. These volcanic rocks mainly show calk-alkaline nature and active continental margin setting. The REE distribution pattern in chondrite-normalized spider diagrams displays a distinct negative slope from LREEs towards HREEs, indicating the enrichment of LREEs compared to HREEs, which is typical of many modern subduction-related volcanic rocks. This and the Primitive Mantle-normalized multi-element patterns also testify to the presence of garnet, hornblende, rutile and plagioclase as residual phases within the source material and low degree of partial melting. Gold mineralization occurs as quartz-sulfide veins (20 cm to 2 m thick) and silicified zones within the highly fractured and brecciated Eocene andesitic rocks, which have been affected by silicic, argillic and sericitic alterations. Au grade reaches >10 ppm in quartz-sulfide veins, while the altered and brecciated host rocks contain about 1.2 ppm Au. The T_h and salinity values measured on the 2-phase liquid-rich fluid inclusions within the quartz sulfide veins range from 176 to 282 °C and 0.65 to 2.6 eq mass % NaCl, respectively, indicating the low salinity and moderate to low temperature of ore-bearing fluids. These values correspond to epithermal mineralization by fluids of mainly meteoric origin upon cooling.

Keywords: Miardan; Epithermal gold; Elementar Geochemistry; Alteration; Fluid inclusion; Microthermometry.

INTRODUCTION

Gold exploration at the periphery of the Pacific Ocean, especially during 1970s, led to the discovery of many high-grade gold deposits related to recent volcanic environments and/or active tectonic settings. Nowadays, these precious metal deposits are known as epithermal, a term introduced by Lindgern (1933) for the classification of ore deposits. Numerous investigations on these ore-forming systems and especially comparing them with active geothermal environments such as White Island volcanic domain at the north of New Zealand (Hedenquist et al., 2000; Cooke and Simmons, 2000) and Ladolam at New Guinea (Simmons and Brown, 2006) show that epithermal deposits mainly are formed at temperatures between 160 and 270 °C and depths of 50-1000 m (pressures below 500 bars). The responsible hydrothermal fluids are dominantly of meteoric origin, while components such as HCl, CO_2 and H_2S are supplied from a magmatic source. Salinities of these fluids are also below 15 eq mass % NaCl (Pirajno, 2009). These deposits occur in the form of veins, stockworks and disseminations within the host rocks.

Epithermal deposits are spatially and genetically associated with porphyry deposits and are classified as two major types of low-sulfidation and high-sulfidation (Hedenquist et al., 2000). These deposits mainly occur within the orogenic belts of Mesozoic to Cenozoic, though some deposits are also related to the Paleozoic orogens.

The Cenozoic Urumieh-Dokhtar magmatic arc (UDMA) is one of the major hosts of the porphyry-epithermal mineralizations in Iran, with about 2000 km length and ~50 km width, which was formed by the northeastward subduction of the Neo-Tethyan oceanic crust beneath the Central Iranian plate as a result of the convergence between African and Eurasian plates during the Late Mesozoic-Early Cenozoic (Alavi, 1994; Stampfli, 2000; Omrani et al., 2008).

The northwestern part of the UDMA is known as the Arasbaran or Ahar-Jolfa metallogenic zone, which extends from south Armenia to the northwest of Iran and presents Cenozoic magmatism and numerous porphyry-skarn-epithermal mineralizations (e.g., Calagari, 2003, 2004; Maghsoudi et al., 2014; Aghazadeh et al., 2015; Simmonds and Moazzen, 2016; Simmonds, 2019; Simmonds et al., 2019). Three epochs of Late Eocene, Middle Oligocene and Early Miocene were introduced by Simmonds et al. (2017) for Cu±Mo and Cu±Au porphyry deposits and the related epithermal mineralizations in the Arasbaran zone. Some examples of epithermal deposits and prospects in this zone are the Masjed Daghi Cu-Au porphyry-epithermal mineralization (Atalou et al., 2017), the epithermal gold deposits of Nabijan (e.g., Jamali et al., 2017) and Zailic-Sarilar (Miranvari et al., 2020), and the skarn-epithermal deposit of Mivehrood (Alirezaei et al., 2016).

The Miardan ore field in northwest Iran is a gold-bearing altered and mineralized zone with an approximate area of 24.1 km^2, located between the longitudes of 46˚ to 46˚ 38´ E and latitudes of 37˚47´ to 37˚49´N. According to the structural classifications of the Iranian territory, this area is part of the Central Iranian domain and the UDMA (Aghanabati, 2004) and represents an epithermal gold mineralization. Twenty six diamond-drillings have been conducted by Rossdrill Geotech. Company in the mineralized area with a total depth of 4169.6 m, providing access to the deeper parts of it and to core samples. This contribution aims to study the lithology, geochemistry, hydrothermal alteration and mineralization in Miardan, as well as the physic-chemical characteristics of the ore-forming fluids in order to determine the genesis of this mineralization.

Geology of the study area

The Late Cretaceous rocks form the basement of the study area, comprising alternations of serpentinized and chloritized basaltic rocks, basic tuffs and gabbro, accompanied by thin-layered marly limestone, sandstone, conglomerate and shale, which have fault contact with each other. Eocene volcanic and pyroclastic units overlie the basement rocks with an unconformity (E^v and E^{it}), which have mainly cropped out in the central part of the area and host the mineralization. Purple-colored porphyritic andesite and trachy-andesite (with some tuff) (E^v) contain plagioclase phenocrysts as the main rock-forming mineral and are overlain by tuff and ignimbrite (E^{it}), which are fine-grained and are characterized by their pale purple to pink color (Figure 1).

Intrusive rocks of granitic, quartz monzonitic and granodioritic composition, as well as dacitic and rhyodacitic domes (OM^d) and rhyolitic dikes of Oligocene age cut the older units in the study area and its environs. Domes and dikes mainly display porphyritic texture. The granitic body has caused alteration and metasomatism within the wall rocks. There are several faults around the mineralized zone, which justify the assumption that hydrothermal fluids originated from a hidden granitic body in the vicinity of Miardan village are responsible for mineralization in this area.

Sedimentary units in the study area mainly include >70 m thick Pliocene conglomerates with intercalations of pumice, sandstone and siltstone, which crop out in the northern and southern parts of the study area. They are loose and bright in color and contain rounded fragments and a muddy matrix, which characterize a shallow zone during Pliocene. Rock fragments within them have rhyodacitic and andesitic composition. Moreover, pumice and lahar units of Pliocene (Pl^p, Pl^{la}) are also present in the eastern section and southeastern part of the area, respectively. In general, Pliocene units overlie the Eocene rocks, covering more than 50% of the study area and post-dating the mineralization (Figure 1). The youngest units are Quaternary sediments, occurring in the form of delluvials, prolluvials and alluvials (Q).

MATERIAL AND METHODS

Field investigations in the study area were performed for identifying and mapping the rock units, alteration and mineralization zones. Sampling was carried out from altered zones and the almost fresh host rocks, both in

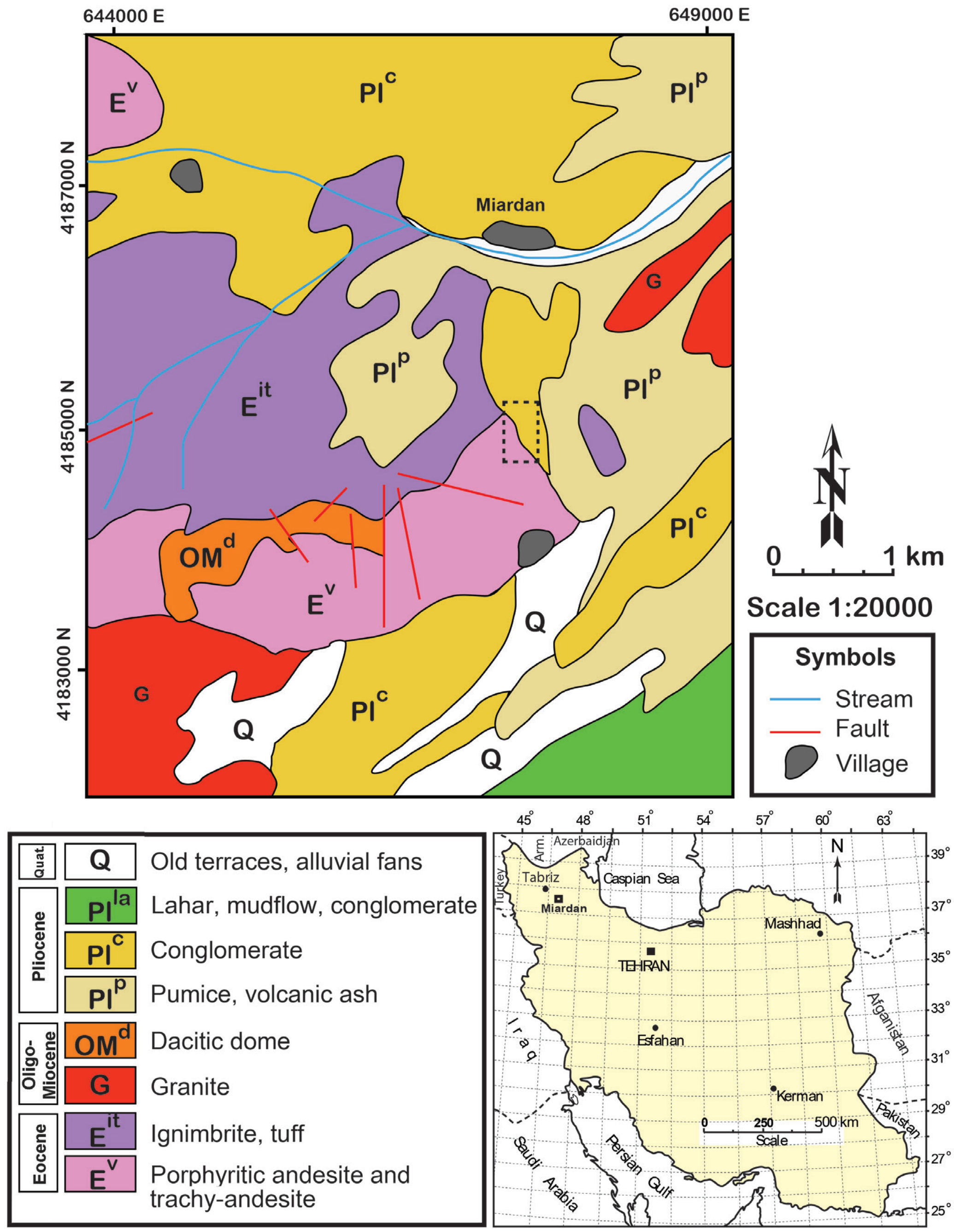

Figure 1. Geologic map of the Miardan area (after Behrouzi et al., 1997), mainly comprised of Cenozoic rock units, and its location in NW Iran. The outline of Figure 5, including the location of the mineralized zone is shown on the map.

surface and in cores. Thirty-one thin sections were prepared for petrographic and mineralogical studies. Moreover, 11 samples of altered rocks from surficial outcrops and diamond-drill cores (each about 5g pulverized sample) were analyzed by X-ray diffraction (XRD) method using *Philips-Xpert Pro instrument* at the Iranian Mineral Processing Research Center (Karaj) to determine the unknown mineral phases within the alteration zones (results in Table 1). Finally, 35 samples of almost fresh rocks were analyzed by ICP-MS (PerkinElmer SCIEX-ELAN DRC-e) in the Zarazma Laboratory (Tehran) for major, minor and trace elements following 4-acid digestion (HF, HCl, $HClO_4$, HNO_3) of pulverized samples (200 mesh particle size, using jaw crusher, disc mill and mortar, respectively), results of which are shown in Table 2.

Fluid inclusion studies were performed on quartz crystals within quartz-sulfide veinlets sampled from surficial outcrops and diamond-drill cores. First, the doubly polished thin sections were examined under a microscope to determine the distribution, shape, size and phase content, genetic and compositional types of fluid inclusions and the species of daughter minerals. After petrographic examination, the wafers of 3 samples were subjected to microthermometric analysis at the University of Isfahan (Iran) using a calibrated THMS600 Linkam heating-freezing stage, equipped with two heating (TP94) and freezing (LNP) controllers, attached to an Olympus petrographic microscope and a monitoring video apparatus. The first and last melting points of ice and homogenization temperature measurements were performed on 27 fluid inclusions. The data were reproducible to ±0.2 °C for freezing runs and ±0.6 °C for heating runs.

RESULTS

Petrography of rock units in Miardan

Microscopic observations show that andesitic and trachy-andesitic rocks associated with alteration zones consist of plagioclase and hornblende phenocrysts set in a microlithic groundmass (Figure 2a). Andesitic lavas sporadically contain dacitic and rhyodacitic intercalations with microlithic texture. Sericite, chlorite and pyrite are the characteristic secondary minerals within them. The XRD analysis has also identified mica (sericite) and chlorite in these rocks (Table 1).

The pyroclastic units are pale-purple andesitic tuffs (Figure 2b). They have perlitic texture and the cavities and open spaces are mainly filled with chlorite and polycrystalline quartz and partly with zeolite. These rocks also show carbonatization. The pumice layers have a clear border with andesites and tuffs and are distinguished by their matrix components (Figure 2c).

The conglomerate units of the Pliocene age overly the Eocene rocks. They are composed of large andesitic and rhyodacitic fragments, lapilli tuff and pumice fragments, as well as volcanic ash. The large diameter of these fragments reaches 1m and the average thickness of this rock unit is between 70 and 100 cm.

The rhyolitic rocks and porphyritic granites are outcropped in the northeastern and southwestern parts of the area and extend beyond the study area. Granite, microdiorite and rhyolitic dikes have intruded the Eocene units. In thin sections, rhyolites display microgranular texture with lesser rounded quartz phenocrysts (Figure 2d). Granite samples have porphyritic texture with fine-grained crystalline groundmass. Their main phenocrysts are medium-sized quartz and plagioclase. Plagioclase phenocrysts have poly-synthetic twinning and some of them are altered to sericite. Quartz crystals in granite are sometimes intergranular and anhedral (Figure 2e).

Table 1. XRD analysis results of the altered ore-host volcanic rocks from (a) diamond-drill cores and (b) surficial outcrops.

(a)	Sample/ Drill hole	Depth (m)	Major minerals	Minor minerals
1	BHB-07	31	Quartz, Feldspar, Dolomite	Chlorite, Mica
2	BHB-03	34	Quartz, Calcite	Chlorite, Mica
3	BHB-03	44	Quartz, Feldspar	Dolomite
4	BHB-07	107	Quartz, Feldspar	Siderite
5	BHB-10	120	Quartz, Feldspar	Chlorite, Mica

(b)	Sample	Alteration zone	Major minerals	Minor minerals
1	BN-426	Supergene argillic	Quartz, Feldspar	Hematite, Kaolinite
2	BN-427	Argillic	Quartz, Feldspar	Sericite, Kaolinite, Montmorillonite
3	BN-428	Silicic/ oxidized	Quartz	Hematite, Jarosite
4	BN-430	Argillic	Quartz	Kaolinite, Montmorillonite
5	BN-431	Supergene argillic	Quartz, Feldspar	Kaolinite,
6	BN-432	Silicified/oxidized	Quartz	Hematite, Kaolinite

Table 2. ICP-MS analysis results of volcanic rocks from the Miardan area. (Dl=Detection limit).

Element	Ag	Al	As	Ba	Ca	Cu	Fe	K	Mg	Na	Nb	P	Pb	Rb	Si	Sr	Ta
Dl	0.1	0.01	0.1	1	0.01	1	0.01	100	100	100	1	10	1	1	0.01	1	0.1
Unit	ppm	%	ppm	ppm	%	ppm	%	ppm	ppm	ppm	ppm	ppm	ppm	ppm	%	ppm	ppm
MS-01	0.4	7.61	5.8	0.1	0.25	13	1.76	68120	1437	1084	18.8	542	38	184	36.23	77.2	0.75
MS-02	0.9	2.61	8.3	508.00	0.10	157	1.47	22485	418	446	6.7	377	123	62	40.60	31.8	0.52
MS-03	0.3	7.63	11.7	0.07	0.33	17	2.32	52589	3214	8806	19.2	607	33	151	35.40	87.2	1.08
MS-04	0.4	8.53	11.5	0.10	0.26	15	2.34	52471	2488	21070	26.9	581	30	134	34.00	104.0	1.26
MS-05	0.1	7.86	4.9	0.09	0.21	25	1.71	74705	1838	1119	18.8	571	19	192	35.25	88.7	1.30
MS-06	0.9	5.22	14.8	0.07	0.20	74	1.49	43247	748	2649	5.9	351	33	99	38.41	83.4	0.42
MS-07	1.0	3.10	42.6	276.00	0.17	18	1.47	14153	1608	<100	4.5	487	28	46	43.04	36.0	0.38
MS-08	0.4	6.94	35.1	562.00	0.38	26	2.07	35791	4355	308	9.8	250	56	112	37.12	44.6	0.65
MS-09	3.5	1.02	10.3	170.00	0.17	109	1.68	7223	530	<100	1.9	263	292	18	44.45	17.8	0.27
MS-10	0.5	2.08	9.3	255.00	0.09	73	1.58	16465	578	<100	3.6	628	276	40	44.04	28.0	0.34
MS-11	0.3	7.97	4.1	0.08	0.26	14	1.94	37660	1829	27698	21.6	351	32	92	33.99	102.0	0.86
MS-12	16.5	2.32	13.3	459.00	0.08	58	2.33	18511	687	262	6.7	255	489	50	42.07	48.6	0.53
MS-13	0.4	1.73	11.7	184.00	0.08	43	1.53	16217	302	273	2.9	147	47	49	43.77	18.8	0.28
MS-14	<0.1	8.22	1.6	559.00	2.41	20	1.49	16586	4911	34635	25.4	296	23	38	32.88	399.0	1.53
MS-15	<0.1	7.61	14.3	0.08	0.40	27	2.11	31634	3550	838	18.8	985	48	132	34.57	90.9	1.33
MS-16	0.1	8.87	42.5	0.23	0.31	29	3.77	35983	3895	1078	41.3	1075	45	134	30.88	84.3	2.55
MS-17	<0.1	7.44	3	0.08	0.25	13	2.12	43670	1609	23183	32.6	457	28	141	34.60	83.6	1.57

Table 2. ... Continued

Element	Ag	Al	As	Ba	Ca	Cu	Fe	K	Mg	Na	Nb	P	Pb	Rb	Si	Sr	Ta
Dl	0.1	0.01	0.1	1	0.01	1	0.01	100	100	100	1	10	1	1	0.01	1	0.1
Unit	ppm	%	ppm	ppm	%	ppm	%	ppm	ppm	ppm	ppm	ppm	ppm	ppm	%	ppm	ppm
MS-18	2.7	2.54	11.2	53.00	0.16	280	1.86	9283	985	<100	5.7	300	1745	31	41.88	16.2	0.49
MS-19	0.3	6.98	5.6	0.06	0.51	26	2.31	29644	6552	21187	20.5	1191	26	84	31.37	129.0	1.33
MS-20	0.4	6.78	16.5	669.00	0.41	28	2.70	35432	3823	182	16.3	1151	26	129	33.28	32.9	1.21
MS-21	0.2	8.39	19.9	782.00	2.76	157	3.15	32468	5974	25806	28.6	2501	13	84	29.70	337.0	1.48
MS-22	1.4	2.36	10.8	401.00	0.11	53	1.35	21222	544	175	6.7	286	972	65	41.50	29.8	0.40
MS-23	<0.1	9.10	7.8	0.07	0.97	6	1.52	41653	3966	26717	49.0	540	45	100	30.00	419.0	2.48
MS-24	0.1	8.31	2.5	561.00	2.23	24	1.79	17234	5274	33628	20.5	318	20	42	31.45	413.0	1.56
MS-25	<0.1	8.03	11.1	57.00	0.59	26	1.46	1256	1583	33413	40.8	1218	6	3	32.13	106.0	2.43
MS-26	0.3	7.69	7.2	0.09	0.30	17	2.32	51296	2612	13567	41.6	603	28	173	31.30	108.0	2.25
MS-27	0.9	1.83	12.3	0.07	0.08	65	1.55	17292	325	236	5.9	265	238	57	39.77	24.3	0.38
MS-28	0.2	7.37	4.0	0.06	0.30	27	2.35	45049	1803	24252	42.0	451	32	150	31.12	99.6	2.43
MS-29	0.2	8.14	7.6	0.06	0.53	29	3.03	45524	5759	16946	41.0	1076	25	149	29.54	102.0	2.38
MS-30	0.3	8.81	2.8	645.00	3.02	38	1.99	14957	6281	32485	19.8	761	33	35	29.21	497.0	1.42
MS-31	0.1	7.86	3.7	527.00	3.09	28	1.52	15992	5171	30864	14.5	465	36	33	30.29	427.0	1.25
MS-32	0.1	8.39	2.2	535.00	2.87	71	2.12	15838	11545	19528	19.7	568	23	31	28.21	496.0	1.52
MS-33	<0.1	8.73	3.6	572.00	2.47	27	1.61	16924	5465	33632	16.8	421	33	47	30.94	453.0	1.36
MS-34	0.1	8.91	5.2	638.00	3.01	30	2.12	17081	6740	33092	18.4	723	31	45	29.11	533.0	1.38
MS-35	4.4	1.17	6.1	50.00	0.10	347	2.10	6650	570	<100	5.1	292	2628	19	40.78	13.4	0.35

Table 2. ... Continued

Element	Th	Ti	U	Zr	La	Ce	Pr	Nd	Sm	Eu	Gd	Tb	Dy	Hf	Er	Tm	Yb	Lu	Y
Dl	0.1	10	0.1	5	1	0.5	0.05	0.5	0.02	0.1	0.05	0.1	0.02	0.5	0.05	0.1	0.05	0.1	0.5
Unit	ppm	ppm	ppm	ppm	ppm	ppm	ppm	ppm	ppm	ppm	ppm	ppm	ppm	ppm	ppm	ppm	ppm	ppm	ppm
MS-01	5.85	4509	2.00	123	43	81	0.05	28.5	6.14	1.35	4.53	0.68	3.81	3.07	2.16	0.28	1.8	0.25	19.60
MS-02	20.10	1212	1.00	32	13	19	6.87	2.5	0.56	0.17	0.05	0.20	0.69	1.20	0.48	<0.10	0.5	<0.10	6.37
MS-03	4.85	4463	1.70	132	29	64	3.41	16.7	4.26	1.01	3.34	0.54	2.75	2.81	1.61	0.21	1.4	0.17	18.40
MS-04	6.63	4657	2.80	208	48	91	8.19	33.6	7.11	1.59	5.06	0.75	4.34	4.15	2.57	0.33	2.1	0.31	25.30
MS-05	2.63	4269	1.20	96	40	72	5.35	23.4	4.78	0.99	3.08	0.51	2.56	2.25	1.53	0.19	1.3	0.13	17.30
MS-06	1.94	3481	2.10	104	26	50	3.03	15.4	3.50	1.00	2.21	0.41	1.95	2.27	1.21	0.16	1.1	0.11	13.20
MS-07	<0.10	1969	1.10	45	10	16	<0.05	1.3	0.79	0.27	0.40	0.22	0.83	1.01	0.57	<0.10	0.7	<0.10	6.80
MS-08	3.54	4757	1.80	131	14	29	0.11	5.7	1.97	0.56	1.47	0.37	1.97	2.65	1.27	0.17	1.2	0.13	14.90
MS-09	<0.10	212	0.60	12	13	<1	<0.05	<0.5	<0.02	<0.10	<0.05	<0.1	<0.02	0.94	0.06	<0.10	0.3	<0.10	2.60
MS-10	<0.10	911	0.90	28	9	10	<0.05	<0.5	<0.02	<0.10	<0.05	0.15	0.32	1.02	0.30	<0.10	0.4	<0.10	4.60
MS-11	5.32	3063	2.70	146	47	68	7.54	30.6	6.30	1.27	4.93	0.79	4.61	3.15	2.47	0.31	1.9	0.28	24.70
MS-12	<0.10	1126	0.80	33	12	17	<0.05	2.5	0.57	0.15	<0.05	0.20	0.65	1.14	0.43	<0.10	0.5	<0.10	6.20
MS-13	<0.10	314	0.50	14	6	4	<0.05	<0.5	<0.02	<0.10	<0.05	0.11	0.08	0.97	0.11	<0.10	0.3	<0.10	3.10
MS-14	5.20	1784	1.30	38	23	29	0.30	3.1	0.71	0.53	0.12	0.18	0.38	1.81	0.22	<0.10	0.3	<0.10	3.70
MS-15	4.86	4120	1.90	38	34	65	6.85	30.4	7.09	1.92	6.63	0.99	5.60	1.31	2.78	0.31	1.7	0.19	26.50
MS-16	6.20	5682	3.37	106	34	64	5.28	23.9	5.27	1.44	4.22	0.71	4.07	2.72	2.16	0.26	1.7	0.21	20.20
MS-17	10.26	3294	3.20	108	39	68	7.14	28.7	6.29	1.10	4.78	0.77	4.62	3.15	2.71	0.36	2.1	0.31	22.10

Table 2. ... Continued

Element	Th	Ti	U	Zr	La	Ce	Pr	Nd	Sm	Eu	Gd	Tb	Dy	Hf	Er	Tm	Yb	Lu	Y
Dl	0.1	10	0.1	5	1	0.5	0.05	0.5	0.02	0.1	0.05	0.1	0.02	0.5	0.05	0.1	0.05	0.1	0.5
Unit	ppm	ppm	ppm	ppm	ppm	ppm	ppm	ppm	ppm	ppm	ppm	ppm	ppm	ppm	ppm	ppm	ppm	ppm	ppm
MS-18	<0.10	1429	0.90	44	8	8	<0.05	<0.5	<0.02	<0.10	<0.05	0.13	0.18	1.38	0.31	<0.10	0.5	<0.10	5.2
MS-19	3.42	4034	2.00	99	30	55	4.35	21.8	4.80	1.38	3.85	0.61	3.37	3.08	1.95	0.26	1.7	0.22	17.5
MS-20	3.46	4522	2.40	116	35	67	5.93	56.4	5.34	1.22	4.19	0.66	3.58	2.89	1.98	0.25	1.6	0.23	19.7
MS-21	4.07	5232	2.70	96	35	64	5.25	24.2	5.05	1.49	3.87	0.58	3.03	2.07	1.61	0.16	1.1	0.10	17.2
MS-22	<0.10	1119	1.16	41	14	20	<0.05	3.2	0.67	0.18	<0.05	0.20	0.68	1.31	0.57	<0.10	0.7	<0.10	6.6
MS-23	9.15	4161	1.40	28	26	55	4.41	20.0	4.37	1.30	2.92	0.56	3.11	1.48	1.93	0.22	1.4	0.14	14.7
MS-24	6.91	1792	1.70	32	24	30	0/35	3.6	0.67	0.50	0.09	0.17	0.33	1.66	0.2	<0.10	0.3	<0.10	3.5
MS-25	7.31	4451	1.10	25	13	24	1.03	9.2	2.23	0.52	2.05	0.45	2.60	1.42	1.51	0.16	1.0	<0.10	1.2
MS-26	8.50	4496	3.10	145	35	69	6.68	28.3	6.50	1.56	4.84	0.73	3.98	3.73	2.39	0.31	2.0	0.30	20.2
MS-27	20.10	798	1.00	29	8	9	<0.05	<0.5	0.12	<0.10	<0.05	0.16	0.42	1.15	0.37	<0.10	0.5	<0.10	5.0
MS-28	11.99	3521	3.20	147	48	73	9.17	37.5	7.53	1.58	5.92	0.91	5.44	4.02	3.29	0.43	2.6	0.40	27.1
MS-29	7.79	5424	2.80	156	40	80	7.3	31.8	7.04	1.68	5.79	0.87	4.97	4.33	3.14	0.40	2.4	<0.16	25.3
MS-30	8.70	2592	2.70	95	31	47	2.25	11.5	2.25	0.87	1.28	0.31	1.20	2.94	0.65	<0.10	0.7	<0.10	7.2
MS-31	7.02	1869	2.50	97	26	39	0.97	6.2	1.19	0.56	0.46	0.21	0.64	2.93	0.37	<0.10	0.4	<0.10	4.7
MS-32	6.10	2616	1.90	105	28	46	2.30	11.2	2.08	0.79	1.21	0.31	1.19	3.08	0.57	<0.10	0.6	<0.10	6.7
MS-33	8.69	2154	2.50	54	28	39	1.58	8.1	1.70	0.74	0.84	0.25	0.96	2.09	0.5	<0.10	0.5	<0.10	6.0
MS-34	8.06	2726	2.84	86	29	45	2.28	11.5	2.17	0.88	1.28	0.31	1.22	2.71	0.66	<0.10	0.7	<0.10	7.3
MS-35	<0.10	763	0.60	24	4	1	<0.05	<0.5	<0.02	<0.10	<0.05	<0.10	<0.02	1.05	0.06	<0.10	0.3	<0.10	2.8

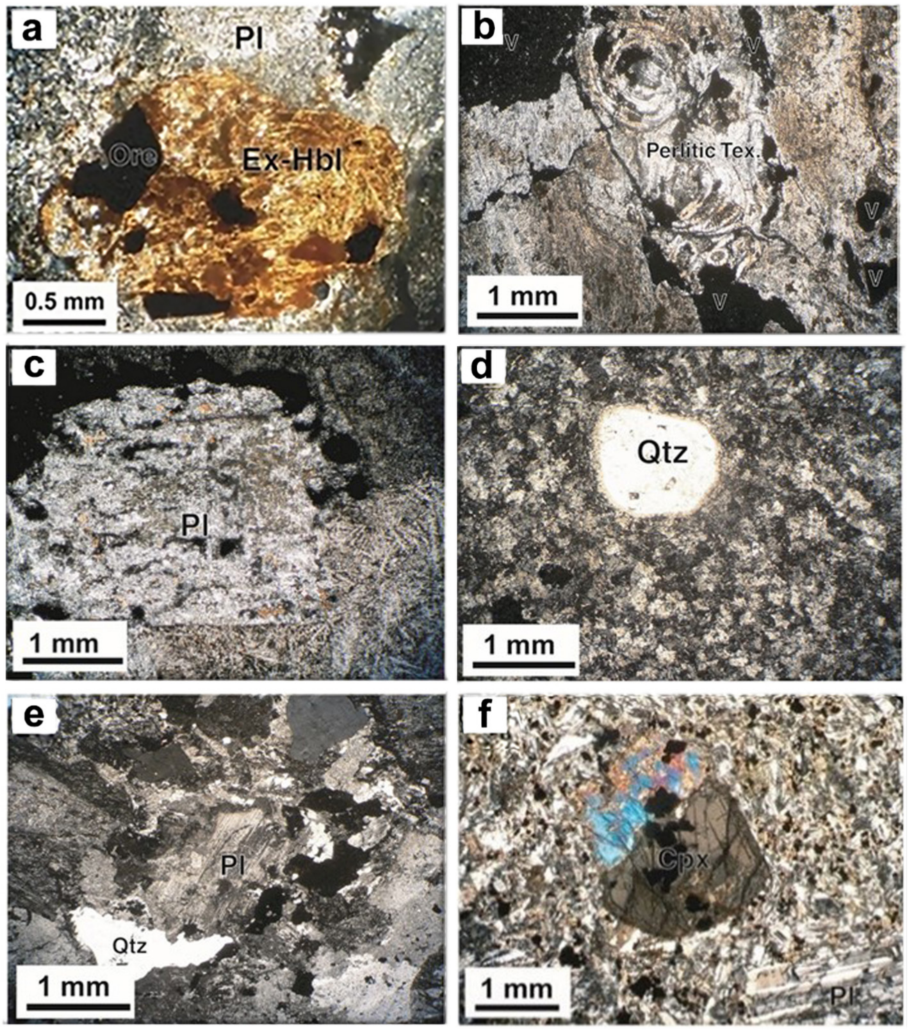

Figure 2. Photomicrographs of magmatic rock units in the study area: (a) andesite with sericitized euhedral plagioclase and the outline of a totally altered euhedral hornblende in a microlithic groundmass, (b) andesitic tuff with perlitic texture, (c) pumice with fragments of igneous rocks, (d) rhyolite with rounded quartz phenocrysts and fine-grained felsitic texture, (e) granite composed of plagioclase and anhedral quartz, (f) microdiorite with clinopyroxene and plagioclase phenocrysts and microlithic groundmass.

The microdioritic rocks show porphyritic texture with fine-grained crystalline groundmass and their main minerals are plagioclase, clinopyroxene (augite) and hornblende (Figure 2f). These rocks exhibit weak sericitic alteration, in which hornblendes have locally been replaced by secondary minerals including tremolite-actinolite, epidote, sericite and calcite.

Geochemical classification of the ore-host volcanic rocks

Since the volcanic rocks of the area have been affected by varying degrees and types of hydrothermal alteration and experienced subsequent mineralogical and geochemical changes, their geochemical classification was performed using less-mobile or immobile elements (Ce, Ta, TiO_2, Y, Nb, Zr). In this regard, based on the ICP-MS analysis data of rock samples (Table 2) and the Winchester and Floyd (1977) diagram, the studied rocks plot within the andesite and trachy-andesite fields (Figure 3). According to the Ce/Yb vs. Ta/Yb diagram (Muller and Groves, 1997), the studied rocks have calk-alkaline nature, while some of them show shoshonitic affinity (Figure 4a). Also, the Th/Yb vs. Ta/Yb diagram (Pearce, 1983) shows that the analyzed samples follow the active continental margin trend and display subduction-related enrichment and crustal contamination (Figure 4b).

Gold mineralization

Gold mineralization in the Miardan area has occurred within the altered and fractured andesitic rocks of Eocene age in a crushed zone, dipping 40-65° to SW (Figures 1 and

5). The gold-bearing zone within the host rocks extends almost vertically and is identified up to depth of 200 m within the diamond-drillings. Based on field and borehole investigations, it is evident that mineralization is associated with minor faults and fractures in the area. The mineralized zone is mainly brecciated and brownish-yellow in color due to the formation of iron oxides/hydroxides following the oxidation of primary sulfide minerals. Many gold-bearing quartz-sulfide veins and veinlets heterogeneously cross-cut the host andesitic rocks, varying in thickness from 20 cm to 2m. Moreover, there are also mono-mineralic and sulfide-bearing quartz veinlets of mm to cm scale (Figure 6). Brecciated and cataclastic structures are evident in all veins and they sometimes contain wall-rock fragments. Based on the paragenesis and physical characteristics, the sulfide-bearing quartz veins/veinlets can be classified into two groups: white-colored quartz veins mainly containing pyrite, and grey-colored veins, which contain a thin layer of sulfide minerals at their walls. The quartz-sulfide veins comprise galena, pyrite, sphalerite and chalcopyrite and lesser barite and martitized magnetite (Figure 6a, b). Due to the presence of three different mineralogical assemblages of oxide, sulfide and sulfate within the veins, three mineralization phases can be proposed for these quartz veins. The oxide phase was separated from the fluid at the beginning of the mineralization process due to the high oxygen fugacity. The second phase, characterized by sulfide minerals, indicates a decrease in the oxygen fugacity of fluid and an increase in sulfur fugacity, leading to the crystallization of these minerals, and the final phase is the depositional phase of barite (sulfate phase). Gold is present not only within the quartz-sulfide veins/veinlets (corresponding to the second phase), but is also found as disseminated particles within the altered and brecciated rocks (Figure 6c). Its grade within the quartz-sulfide veins/veinlets reaches >10 ppm, while it is about 1.2 ppm within the brecciated rocks.

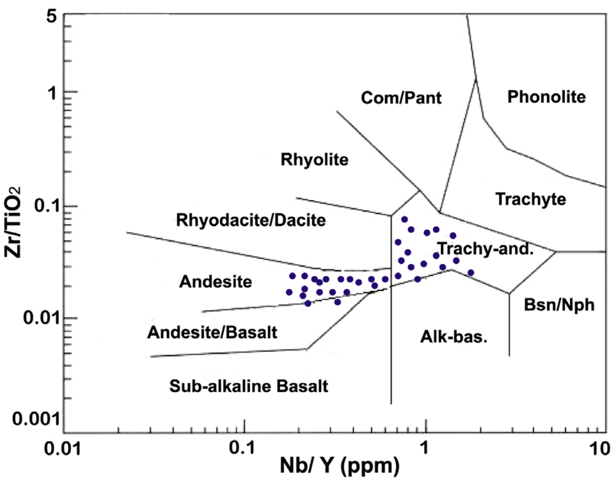

Figure 3. Geochemical classification of the ore-host volcanic rocks in Miardan area (Winchester and Floyd, 1977); data points fall within the andesite and trachy-andesite fields.

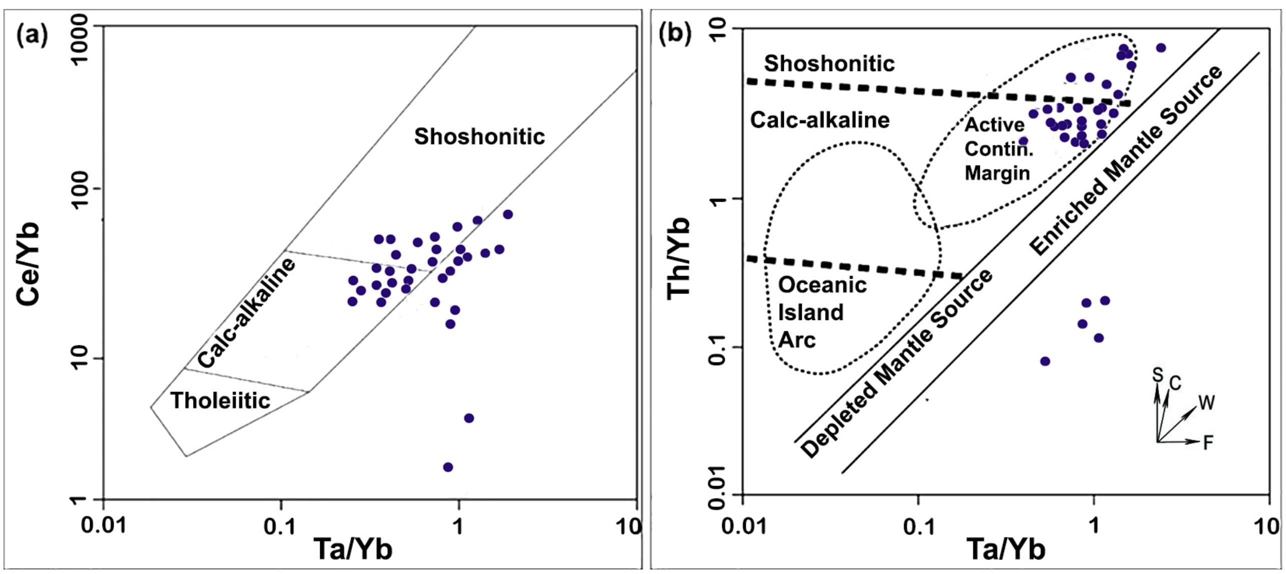

Figure 4. (a) K-index determination diagram for igneous rocks (Muller and Groves, 1997); the analyzed samples mainly plot in the calk-alkaline field, with some showing shoshonitic affinity. (b) Th/Yb vs Ta/Yb diagram (Pearce, 1983); the analyzed samples of volcanic rocks plot within the active continental margin field and show subduction-related enrichment and crustal contamination (C: Crustal contamination, S: Subduction zone enrichment, W: Within-plate enrichment, F: Fractional crystallization).

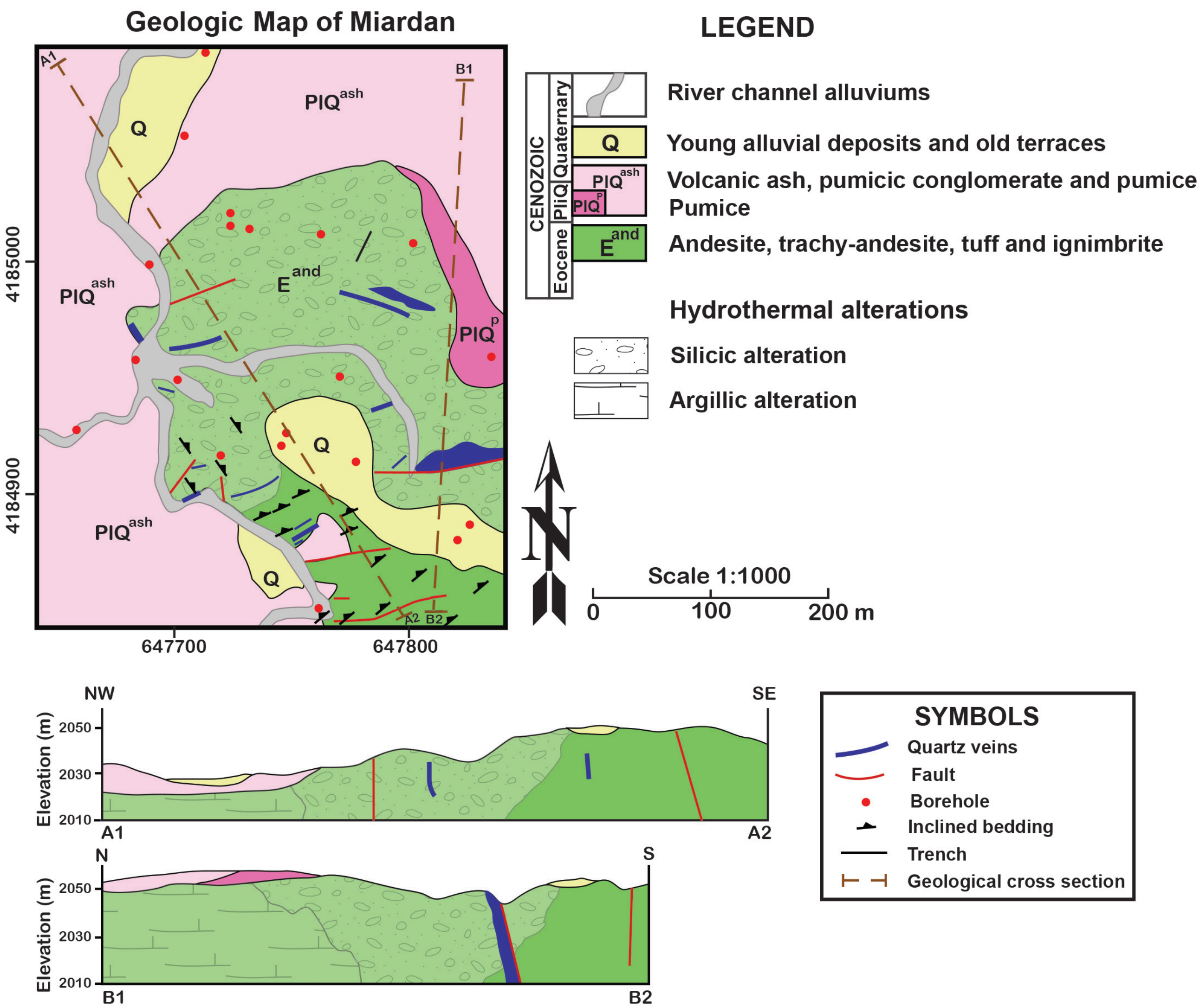

Figure 5. 1:1000 geologic map of the mineralized zone in Miardan (Jahan Zarjouyan Arasbaran Co., 2018) showing the surficial and cross-sectional distribution of hydrothermal alterations and quartz veins.

Hydrothermal alterations

Silicic alteration

Silicification has extensively occurred in the Miardan area. Silica deposited by ore-bearing fluids within the fractures and micro-fractures, forming silicified zones and many quartz and quartz-sulfide veins and veinlets with mm to m scale thicknesses (Fig. 7 a,b). Moreover, silica fills the open spaces of the host rocks (Figure 7c). Groundmass of the andesitic rocks is also intensely silicified (Figure 7d), which is also supported by XRD data.

Sericitic alteration

This alteration is evident both in surficial outcrops and in diamond-drill cores. Petrographic studies show the presence of sericite, with lesser quartz and pyrite in this alteration (Figure 7e). Sericite (20-50 vol%) occurs as fine flakes replacing feldspars and to lesser extent, ferromagnesian minerals such as biotite. This alteration is very intense in some parts, inasmuch as only relicts of plagioclases are observable.

The secondary quartz is fine to medium-grained and anhedral (15-30 vol%), mainly being formed within the rock groundmass. Quartz also occurs as veins of mm to cm scale in this zone. These veins contain pyrite and show brecciated, crustal, mosaic, cockade and druzy textures. These veins often display evidence of crushing and brecciation with various intensities. Pyrite (5-10 vol%) is present as euhedral to subhedral crystals, disseminated within the rock or veins, as well as within or adjacent to

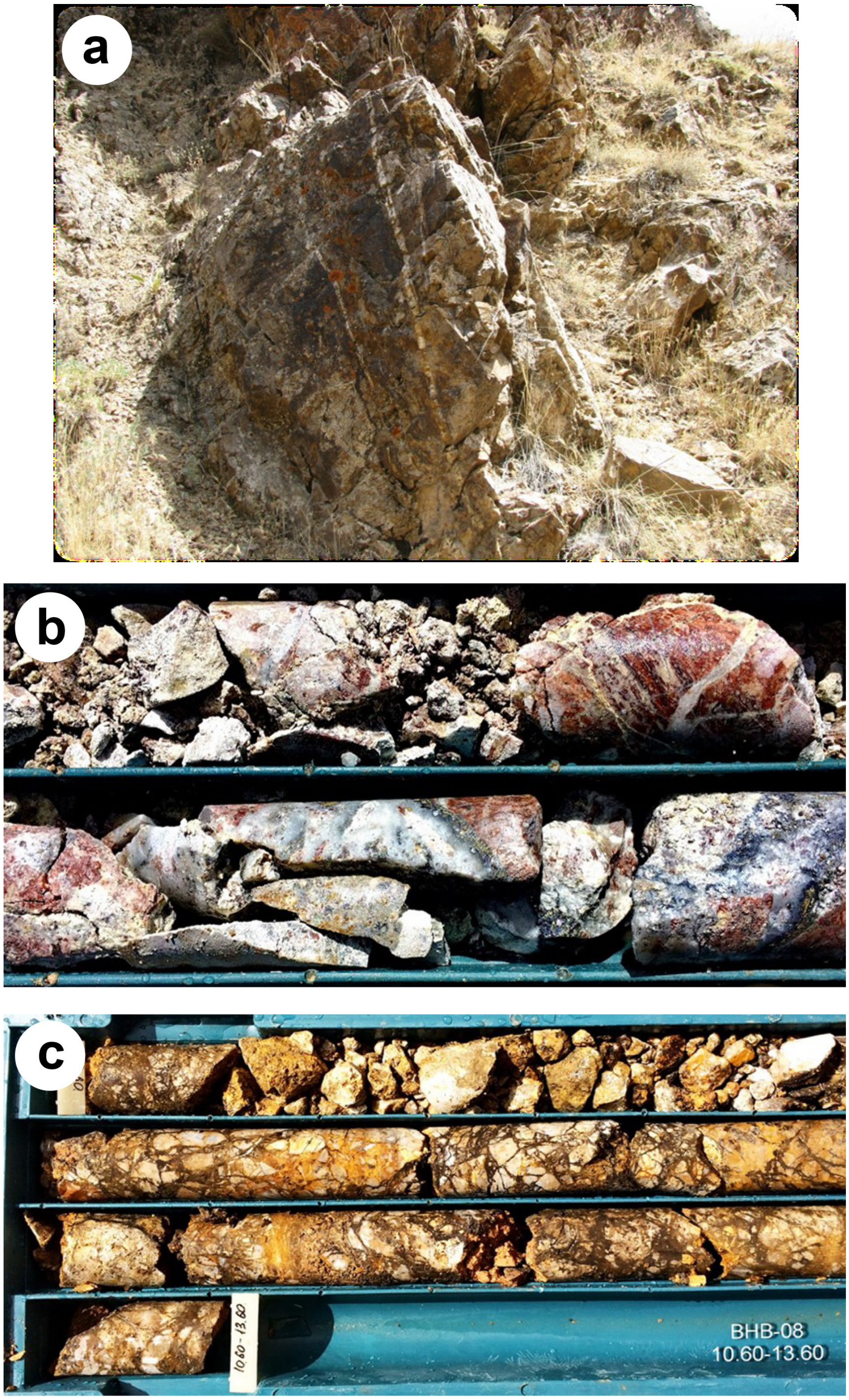

Figure 6. (a) Outcrop of quartz veins in the Miardan area. (b) Quartz veins containing pyrite, chalcopyrite, sphalerite, galena and gold within the andesitic rocks; gold grade is >10 ppm; BHB-20-52.5/49-5.55 cores. (c) Gold-bearing breccia with gold grade of 1.2 ppm; the bright-colored fragments are metasomatized host rocks containing quartz and sericite, and the brown colored parts contain quartz and iron hydroxide.

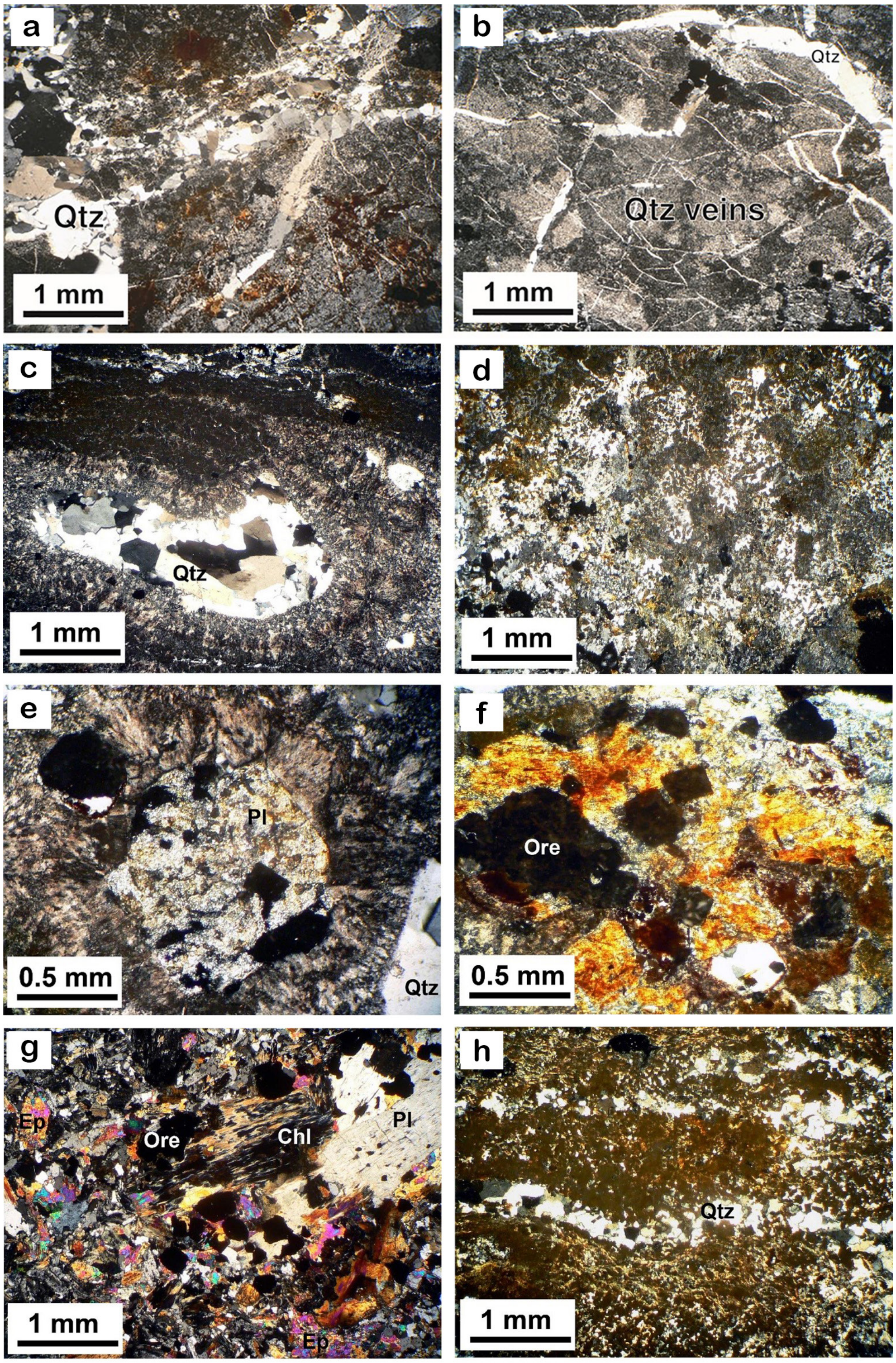

Figure 7. Photomicrographs of hydrothermal alterations within the andesitic rocks; (a) and (b) quartz veinlets of various thicknesses within the host rocks, (c) open-space filling with quartz, (d) intense silicification of the host rocks, superimposed by later supergene alteration, (e) sericitic alteration affecting feldspars of the andesitic rocks, (f) argillic alteration, along with later supergene alteration of euhedral pyrites, (g) propylitic alteration with the formation of chlorite and epidote, (h) oxidation of primary sulfide minerals disseminated within the host rock during the supergene alteration.

altered ferromagnesian minerals, such as amphibole and biotite.

In general, this type of alteration has occurred both selectively and pervasively. In the selective type, plagioclases are altered into sericite, while mafic minerals (biotite and amphibole) are replaced by chlorite. But in pervasive alteration all minerals have been replaced by sericite.

Argillic alteration

This alteration zone has limited surficial outcrops and is locally observed in diamond-drill cores. At depth, this alteration occurs near fractures, faults and areas of high permeability, as it requires more acidic leaching. Hand specimens from this zone are greyish white in color. The most important characteristic of this alteration zone is the formation of clay minerals (kaolinite and montmorillonite; Table 1), along with lesser amounts of sericite. Petrographic studies show that plagioclase crystals have been completely converted to clay minerals, leaving only some relicts; moreover, clay minerals have also been formed within the groundmass (Figure 7f). Sericite is only partially observed. Quartz is disseminated as fine anhedral grains within the groundmass. Pyrite is present in small amount in this zone.

Propylitic alteration

Limited evidence of this alteration is found in the volcanic rocks of the region, distal to the intrusive bodies. Feldspars have partially replaced by epidote, chlorite and lesser sericite. All amphiboles (hornblende) have been altered to chlorite and calcite, while biotite phenocrysts have been altered to chlorite, inasmuch as only relicts of primary minerals have been left. Lesser amounts of pyrite are also present in this zone (<2 vol%).

Epidote occurs as fine-grained crystals, mainly in and around the plagioclase and ferromagnesian minerals, whereas chlorite substitutes ferromagnesian minerals (Figure 7g). Furthermore, chlorite and epidote, together with calcite form veinlets in this zone. Calcite is present in veinlets, and is also disseminated within the rock groundmass (adjacent to and within the altered plagioclase and amphibole crystals).

Supergene alteration

Oxidized and leached Zone

Due to the presence of pyrite and aluminosilicate minerals in the sericitic alteration zone, the descending surface waters become acidic upon weathering and oxidation of these minerals, causing intense leaching of the host rocks and formation of clay minerals (mainly kaolinite) along with hematite and jarosite (Table 1 and Figure 7h). The supergene oxidized and leached zone is developed in the surficial parts of study area, where hematite and goethite are the dominant phases.

Fluid inclusion studies

Petrography

Quartz crystals within both white and grey-colored quartz veinlets at Miardan contain fluid inclusions as randomly distributed relatively large-sized ones (up to 40 μm in size) and numerous cross-cutting trails of smaller inclusions (Figure 8). The observed inclusions have round, irregular and negative crystal shapes in order of abundance (Figure 8). Necking-down is evident in some inclusions (Figure 8b).

Most of the inclusions in quartz range in size from 10 to 40μm. The randomly distributed, relatively larger inclusions with rather similar phase ratios (e.g., Hedenquist et al., 1998; Wanhainen et al., 2003; Bodnar, 2003; Goldstein, 2003; Seedorff and Einaudi, 2004; Bouzari and Clark, 2006; Simmonds et al., 2015) with no trails of secondary inclusions cross-cutting them were considered as primary, while smaller ones oriented along the healed micro-fractures of host crystals were considered as secondary inclusions. Some of these secondary inclusions are found along the micro-fractures confined within the host crystals and can be considered as pseudo-secondary inclusions.

Based on the phase content at room temperature, almost all of the observed inclusions are two-phase liquid-rich (aqueous) (Figure 8), which were homogenized to liquid phase during heating. The estimated degree of fill (the volumetric proportion of liquid to the total volume of the inclusion) for these inclusions is about 0.7-0.8. No recognizable CO_2-bearing inclusion was observed within the studied sections. The lack of daughter minerals such as halite in these fluid inclusions indicates that the salinity of these fluids is less than 26 eq mass % NaCl, testifying to moderate to low salinity (Roedder, 1984), which can be caused by mixing with meteoric waters (Barnes, 1979).

Fluid inclusion Microthermometry

Homogenization temperature

Heating experiments were conducted on liquid-rich two-phase inclusions. All of these inclusions were homogenized into liquid state by disappearance of vapor bubble; the measured T_h(LV→L) values range from 176 to 282 °C (Figure 9a). The highest frequency of homogenization temperatures is in the range of 170-200 °C, with another set of data clustering in the range of 270-290 °C.

Salinity determination

Freezing-based salinity measurements were principally carried out on liquid-rich 2-phase inclusions. Samples were rapidly cooled down to about -100 to -110 °C to

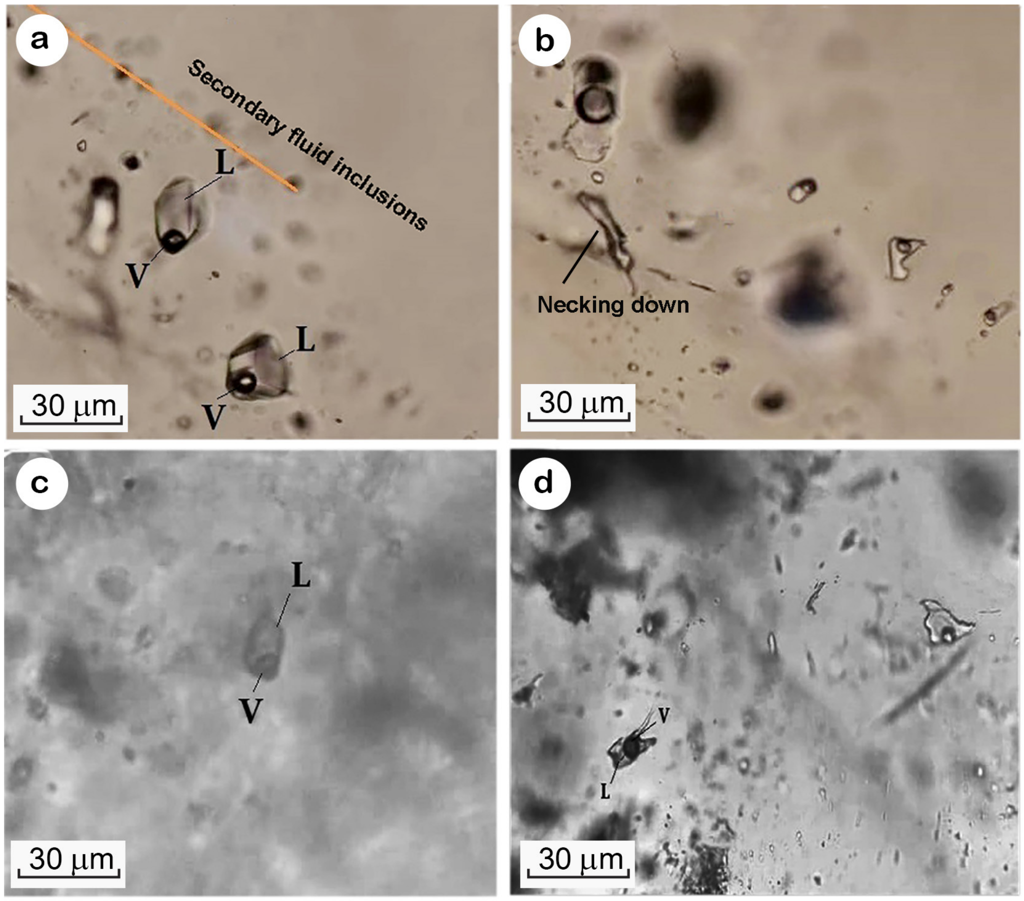

Figure 8. Photomicrographs illustrating fluid inclusions within the quartz veins from Miardan. (a) Negative crystal and irregular shaped 2-phase inclusions, (b) irregular shapes and necking down among the studied inclusions, (c) a large separate primary 2-phase (L+V) fluid inclusion, (d) irregularly shaped primary 2-phase (L+V) fluid inclusions.

detect the possible formation of chlathrate, ice, salt hydrates and carbonic solid phase. Upon progressive heating, the eutectic melting (T_e), last ice melting [T_m(ice)] and total homogenization [T_h(LV→L)] temperatures were measured. The first melting point for ice (T_e) was about -22 °C, based on which it can be conceived that the main salt within these inclusions is NaCl, with lesser KCl (Borisenko, 1977). The bulk salinity of the fluid was calculated from T_m(ice) (Bodnar, 1993) using AqSo WHS software (Bakker, 2012).

The last melting point of the ice was about -0.3 to -1.6 °C. The calculated values of 0.65-2.6 eq mass % NaCl indicate the low salinity of the fluids (Figure 9b). Most of the salinity data cluster between 1.5 to 2.5 eq mass % NaCl (Figure 9b). The lack of halite daughter mineral in the studied fluid inclusions is due to the fact that halite saturation occurs when salinity is >26 eq mass % NaCl at 25 °C (Roedder, 1984).

DISCUSSION

Formation conditions of hydrothermal alterations

Factors causing silica deposition from hydrothermal fluids as quartz veins/veinlets and also as silicic alteration within the host rocks include a decrease in pressure, temperature and pH of hydrothermal fluids. The sericitic alteration occurs in almost all rocks rich in aluminosilicates, which have been affected by acidic fluids (Van Middelaar and Keith, 1990). The decrease in temperature and a(K^+)/a(H^+) of the magmatic fluids leads to the formation of sericite as the dominant potassium silicate phase in the phyllic alteration stage (Hemley and Hunt, 1992). Thus, during these reactions, plagioclase is replaced by sericite at low pH and under the influence of potassium metasomatism and hydrolysis. Secondary quartz is also formed by this reaction, either dispersed within the groundmass or as veinlets. According to this reaction, Na^+ ions are released during the conversion of albite to sericite, which are completely removed from the

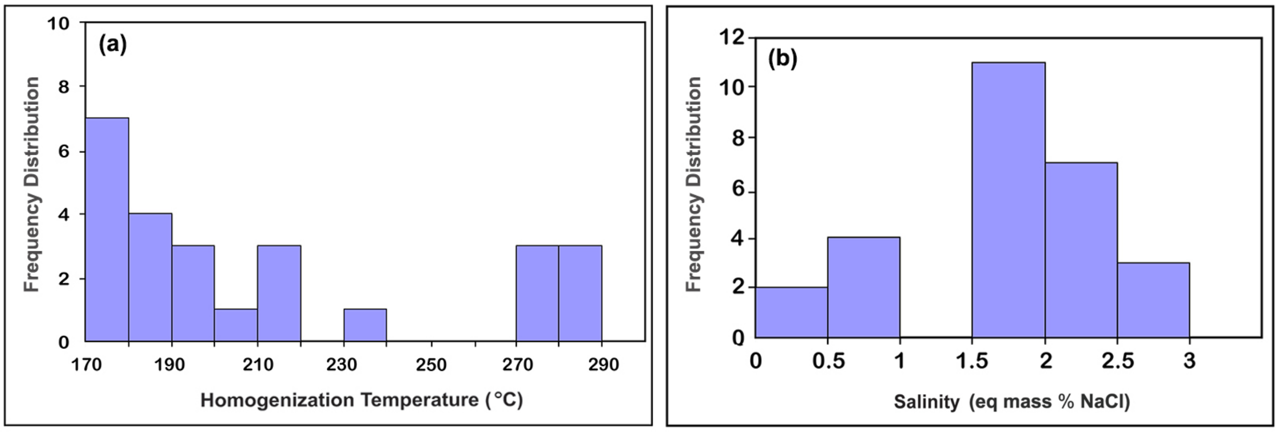

Figure 9. Frequency distribution of the measured (a) homogenization temperatures and (b) salinities of fluid inclusions within the quartz veins at Miardan.

altered rock by the altering fluids. Alkali feldspars are also replaced by sericite at low pH due to hydrolysis, which also produces silica, while the released potassium ions can be used to convert plagioclase to sericite. The effects of sericitization are also visible in the ferromagnesian minerals, during which Na, Ca and Mg are released and removed from the altered rock.

Argillic alteration occurs under relatively high acidity and high water/rock conditions (Titley and Beane, 1981), during which Al is immobile. Ascending of acidic volatiles (containing HF, HCl and SO_2) from the cooling intrusive bodies and their mixing with low-temperature meteoric and surface waters leads to the development of a low pH condition and hence, intense leaching of the surrounding rocks and formation of argillic alteration. Intense hydrolysis of aluminosilicates under such acidic conditions leads to the formation of clay minerals (Montoya and Hemley, 1975), during which Na, K, Ca and Mg are removed from the subjected rocks, while H_2O and SiO_2 are added. This alteration typically occurs at temperatures below 250 °C through H^+ metasomatism (Robb, 2005).

Geochemically, the propylitic alteration is developed under weak H^+ metasomatism (leading to the formation of montmorillonite) to intense Mg or Na metasomatism (resulting in the substitution of feldspars by magnesium chloride, Mg-Fe carbonate or Na-rich alkali-feldspars). Elements such as Mg, Ca, Fe, S, CO_2 and water, along with lesser amounts of K must be added to the rock during this alteration. In general, fluids responsible for this alteration are mixtures of magmatic and meteoric waters (Simmons et al., 2000; Sillitoe, 2000). Mg^{2+}, Fe^{2+}, Ca^{2+} and K^+ are supplied by the destruction of primary minerals, especially ferromagnesian minerals and feldspars, while CO_2, H_2O and S are supplied by hydrothermal fluids or groundwater. The temperature range of this alteration is between 200 and 350 °C, while the water/rock ratio is low (Robb, 2005).

Finally, the most important reactions in the supergene oxidized and leached zone are oxidation, hydrolysis and hydration, which lead to the oxidation of sulfide minerals and kaolinization of feldspars and micas.

Geochemistry of REEs and trace elements within the host andesitic rocks

The geochemical analysis data of the host andesitic rocks show that REE contents in the analyzed samples range from 0.16 ppm to 80 ppm. According to Figure 10, the highest LREE content of 43.38 ppm belongs to the Ce, and the highest HREE content of 12.38 ppm belongs to Y.

The overall distribution pattern of REEs relative to the chondrite (Sun and McDonough, 1989; Figure 11a) for the ore-host rocks shows a distinct negative slope from LREEs towards HREEs, revealing a fractionated feature with a flat trend for HREEs, and enrichment of LREEs compared to HREEs, which is similar to the typical pattern of many modern subduction-related volcanic rocks (Martin, 1999). Moreover, this pattern may testify to the presence of garnet as a residual phase within the magma source materials (Rapp et al., 1991; Wolf and Willie, 1994; Zamora, 2000). On the other hand, the flat pattern of HREEs suggests that amphibole was also present in the magma source region. Therefore, the low HREE abundance reflects the presence of garnet ± hornblende in the residue of the source materials following their partial melting (e.g. Simmonds, 2013). Residual garnet can only exist at high pressures, so it can be concluded that the pressure in the source region was high, because magmas derived from low-pressure garnet systems have a flat REE pattern without HREE depletion. Eu does not show considerable depletion and negative anomaly, which may be attributed to the lack of plagioclase as a residue in the

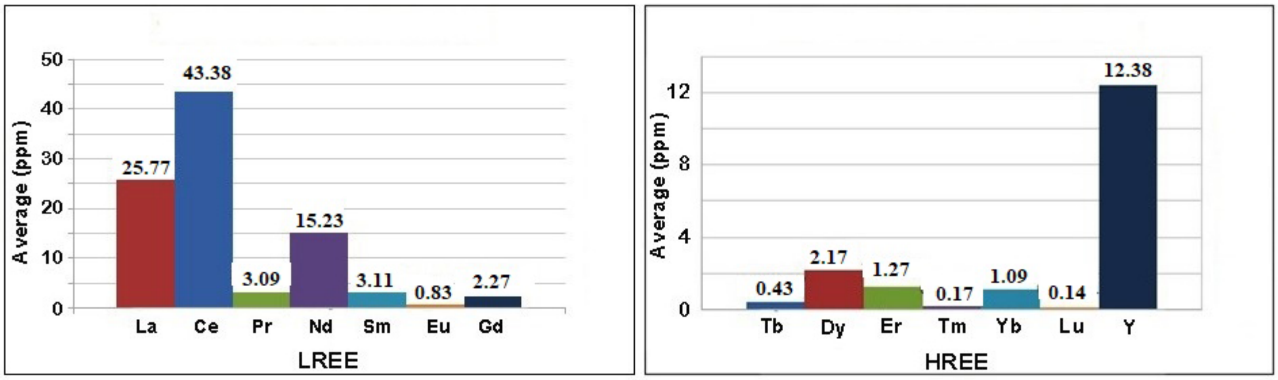

Figure 10. Histograms showing the average REE contents of andesitic rocks in the Miardan area.

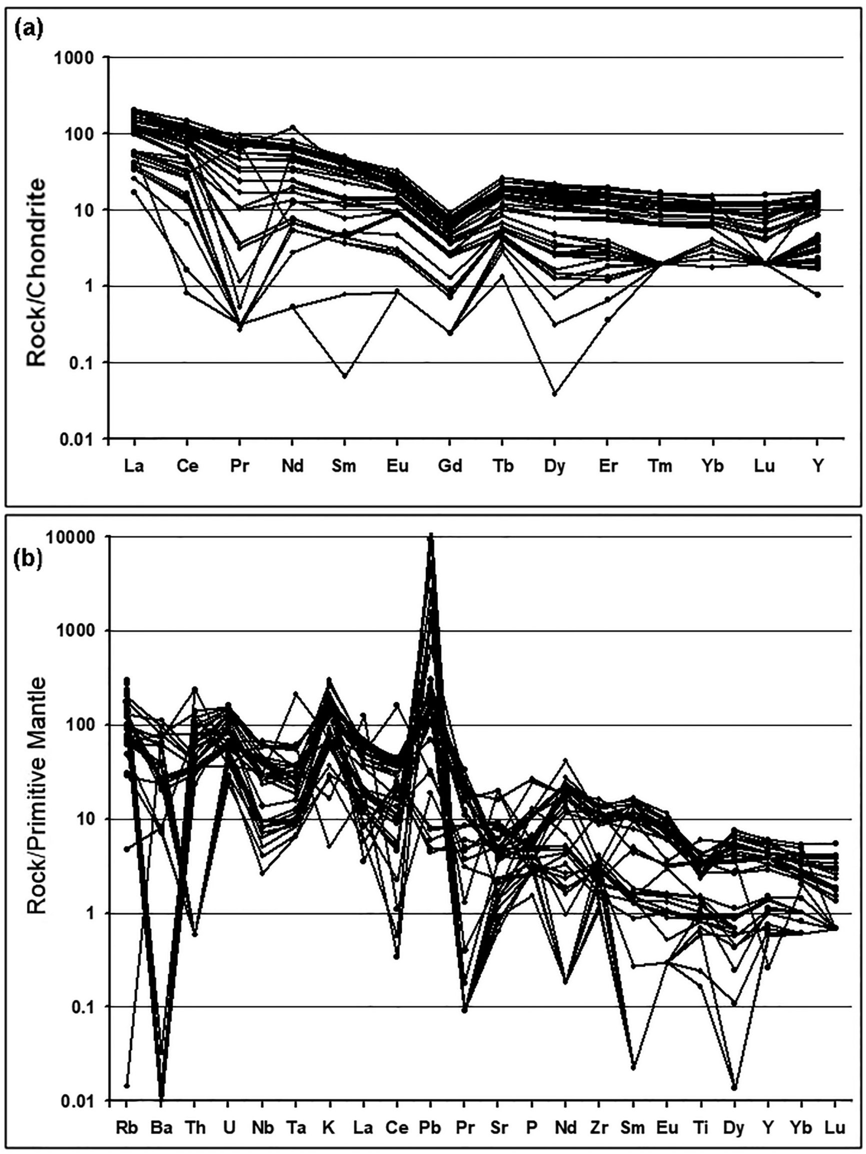

Figure11. (a) Chondrite and (b) Primitive Mantle-normalized (Sun and McDonough, 1989) distribution patterns of REEs, and the minor and trace elements (respectively) in the studied andesitic rocks of Miardan area.

magma source region, though the presence of hornblende as restite in the magma source region may negate the influence of the residual plagioclase (Rollinson, 1993). On the other hand, the negative anomalies of Pr and Gd can be attributed to the differentiation of clinopyroxene and hornblende (Rollinson, 1993).

Trace element contents of the host rocks were normalized relative to the primitive mantle (Sun and McDonough, 1989), the distribution pattern of which is shown in Figure 11b, with an overall decreasing trend from Rb to Lu. LREEs and LILEs show distinct enrichment, while HFSEs show depletion. As shown in Figure 11b, Rb, Pb, K, U and Nd show positive anomalies and Nb, Ti, Ba, Sr and Ce show negative anomalies. Negative Nb-Ta-Ti anomalies are caused by the presence of Fe-Ti oxides (rutile, ilmenite) or hornblende as residual minerals in the magma source region (Martin, 1999) since these minerals are known as the main repositories of HFS elements. These negative anomalies also suggest that melting occurred under high pressure conditions (>1.5 GPa) (Barth et al., 2002), so that rutile remained as a restite mineral. Therefore, strong negative Nb anomaly and weak negative Ti anomaly, along with no depletion of Zr or Hf may testify to a small amount of residual rutile in the magma source material (Martin, 1999), in turn indicating a low to moderate partial melting at higher pressures (Rapp et al. al., 1991).

The enrichment of Rb and K may be related to the metasomatism of mantle materials or contamination by continental crust. This enrichment can also be related to the formation of clay minerals and sericite. The negative anomalies of P, Sr and Ba indicate the role of continental crust in magma evolution or fractional crystallization (White and Chappel, 1983; Chappel and White, 1992; Pe-Piper et al., 2002). Intense Sr depletion can be attributed to the presence of plagioclase as a residual phase in the source region. Then, the lack of significant Eu anomaly was resulted from the negating effect of residual hornblende (Rollinson, 1993). Alteration of plagioclases in some of the analyzed samples can also enhance the Sr depletion. The high Pb content and its intense positive anomaly are characteristic of subduction environments, being produced by dehydration of the subducting oceanic slab, as well as through mantle wedge interactions. Thus, the intense positive anomaly of Pb in the studied samples can be attributed to its high mobility within the fluids produced at such settings (Brenan et al., 1995; You et al., 1996; Juteau and Maury, 1997), although the occurrence of galena mineralization by hydrothermal solutions should not be neglected, which is confirmed by field and microscopic studies. In subduction environments, Ba, Th, Ce, P, Sm and Sr can be mobile (Pearce, 1983). The negative Ce anomaly in the primitive mantle-normalized diagram is probably the result of the mobility of this element during the subduction process. The enrichment of LILEs and LREEs in comparison with HREEs (such as Yb) can be attributed to subduction of sediments and the associated fluids in continental margin settings (Floyd and Winchester, 1974). The enrichment of LILEs is attributed to the high solubility of these elements in chlorine-rich aqueous solutions, which can be easily transported by solutions produced from the subducting slab. However, the solubility of HFSEs in such solutions is low and thus, they are depleted in subduction related fluids and magmas (Kepler, 1996).

Finally, it can be concluded that the geochemical properties of the studied rocks indicate low-degree partial melting of the source materials at high pressure and the presence of some hornblende, garnet, plagioclase and rutile as residual phases. In addition, the distribution pattern and enrichment of LREEs in calk-alkaline rocks of northwest Iran indicate that these rocks may have originated from the upper mantle, rich in these elements (Rio et al., 1981).

Eu and Ce anomalies

The Eu and Ce anomaly values were calculated using the data obtained from ICP-MS analysis using the following equations (Rollinson, 1993), the results of which are listed in Table 3.

$$Eu/Eu^{*}=Eu_n/\ [(Sm_n \cdot Gd_n)^{1/2}]$$
$$Ce/Ce^{*}=Ce_n/[(La_n \cdot Pr_n)^{1/2}]$$

Whenever the Eu/Eu* and Ce/Ce* values are greater than one, they display a positive anomaly (Sun and McDonough, 1989) and imply the oxidizing nature of the magma. The Eu/Eu* values for the Miardan andesitic rocks are mainly above 1, and only a few samples show a weak negative anomaly. The negative Eu anomaly is characteristic of subduction-related calk-alkaline magmas, indicating the presence of plagioclase in the residual phase during partial melting (Yang and Li, 2008). Because of the ionic similarity of Eu^{2+} with Ca^{2+}, Eu can replace Ca within the plagioclase structure. However, Rollinson (1993) states that the presence of large amounts of restite hornblende in the source region counteracts the effect of residual plagioclase on negative Eu anomaly. On the other hand, since Eu/Eu* is calculated on the basis of Eu abundance compared to the concentrations of Sm and Gd, the higher values of the Eu anomaly can be attributed to the fact that a smaller fraction of Eu was available for altering hydrothermal fluids, compared to Sm and Gd (Giese and Bau, 1994; Giese et al., 1993; Simmonds et al., 2011). Thus, while these two elements were washed and removed during alteration, less Eu was removed, resulting in higher Eu/Eu* values. Finally, Eu is immobile

Table 3. Eu/Eu* and Ce/Ce* anomaly values of the studied samples.

Sample number	Eu/Eu*	Sample number	Eu/Eu*	Sample number	Ce/Ce*	Sample number	Ce/Ce*
MS1	0.78	MS20	0.78	MS1	12.94	MS20	1.08
MS2	3.10	MS21	1.02	MS2	0.47	MS21	1.10
MS3	0.81	MS23	1.11	MS3	1.50	MS23	1.20
MS4	0.81	MS24	6.22	MS4	1.07	MS24	2.42
MS5	0.78	MS25	0.47	MS5	1.15	MS25	1.53
MS6	1.09	MS26	0.85	MS6	1.31	MS26	1.05
MS7	1.46	MS28	0.72	MS8	5.47	MS28	0.81
MS8	1.00	MS29	0.80	MS11	0.84	MS29	1.09
MS11	0.69	MS30	1.56	MS14	2.58	MS30	1.31
MS14	5.54	MS31	2.31	MS15	1.00	MS31	1.81
MS15	0.85	MS32	1.52	MS16	1.11	MS32	1.34
MS16	0.93	MS33	1.89	MS17	0.95	MS33	1.37
MS17	0.61	MS34	1.61	MS19	1.12	MS34	1.29
MS19	0.98						

in oxidized conditions and will be concentrated through surface adsorption by oxides or clay minerals during supergene alteration.

The Ce/Ce* ratio in the studied samples is mainly above 1 and indicates again the relatively high oxygen fugacity during crystallization of the andesitic rocks (Rollinson, 1993). Only a few samples have a slightly negative anomaly, indicating the removal of some Ce as Ce^{3+} by altering and ore-forming fluids. As the stability of REE-bearing complexes increases with increasing temperature (Wood, 1990; Haas et al., 1993), negative values can represent zones exposed to higher temperature fluids.

Interpretation of microthermometric data

Based on the T_h versus salinity plot (Figure 12a), a low to moderate temperature and low salinity fluid was responsible for mineralization at Miardan, showing a simple cooling trend in this diagram, which testifies to the deposition of gold and accompanying minerals due to the decrease in fluid temperature and the instability of Au-transporting complexes. Moreover, the minimum vapor pressure at the time of trapping was generally less than 50 bars for the analyzed inclusions and only a small number of fluids inclusions, which had a high homogenization temperatures (270-290 °C), show a minimum vapor pressure of about 50 to 70 bars. The obtained homogenization and salinity values correspond well to the epithermal deposits (Wilkinson, 2001; Figure 12b), for which the fluid temperatures are below 300 °C and the salinity is below 5 eq mass % NaCl.

Density calculations for the studied inclusions were carried out according to Zhang and Frantz (1987) based on which, the studied fluid inclusions show densities of 0.7-0.9 g/cm^3 (Figure 12c). Finally, according to the T_h vs salinity diagram provided by Kesler (2005), the ore-bearing fluids had meteoric water origin (Figure 12d).

CONCLUSION

Field and petrological studies show that the Miardan area is generally composed of volcanic rocks and is covered by volcaniclastic and tuff units. Gold mineralization in the Miardan area is found within the altered, fractured and brecciated andesitic rocks of Eocene age, which also contain iron oxides/hydroxides due to the oxidation of primary sulfide minerals, particularly pyrite. In this area, andesitic rocks are cross-cut by numerous white and milky-colored quartz-sulfide veins and veinlets, as well as grey-colored quartz veins that contain a thin layer of sulfide minerals in the margins (pyrite, chalcopyrite, sphalerite and galena), within which the gold content reaches higher than 10 ppm. In addition to quartz veins, gold is also found as disseminations within the altered and brecciated rocks with an approximate Au grade of 1.2 ppb.

Supergene and hypogene alterations are widespread in the Miardan area. Hypogene alterations include silicification, as well as sericitic, argillic and propylitic zones. Supergene alteration has also caused kaolinization, oxidation and leaching of host rocks and quartz-sulfide

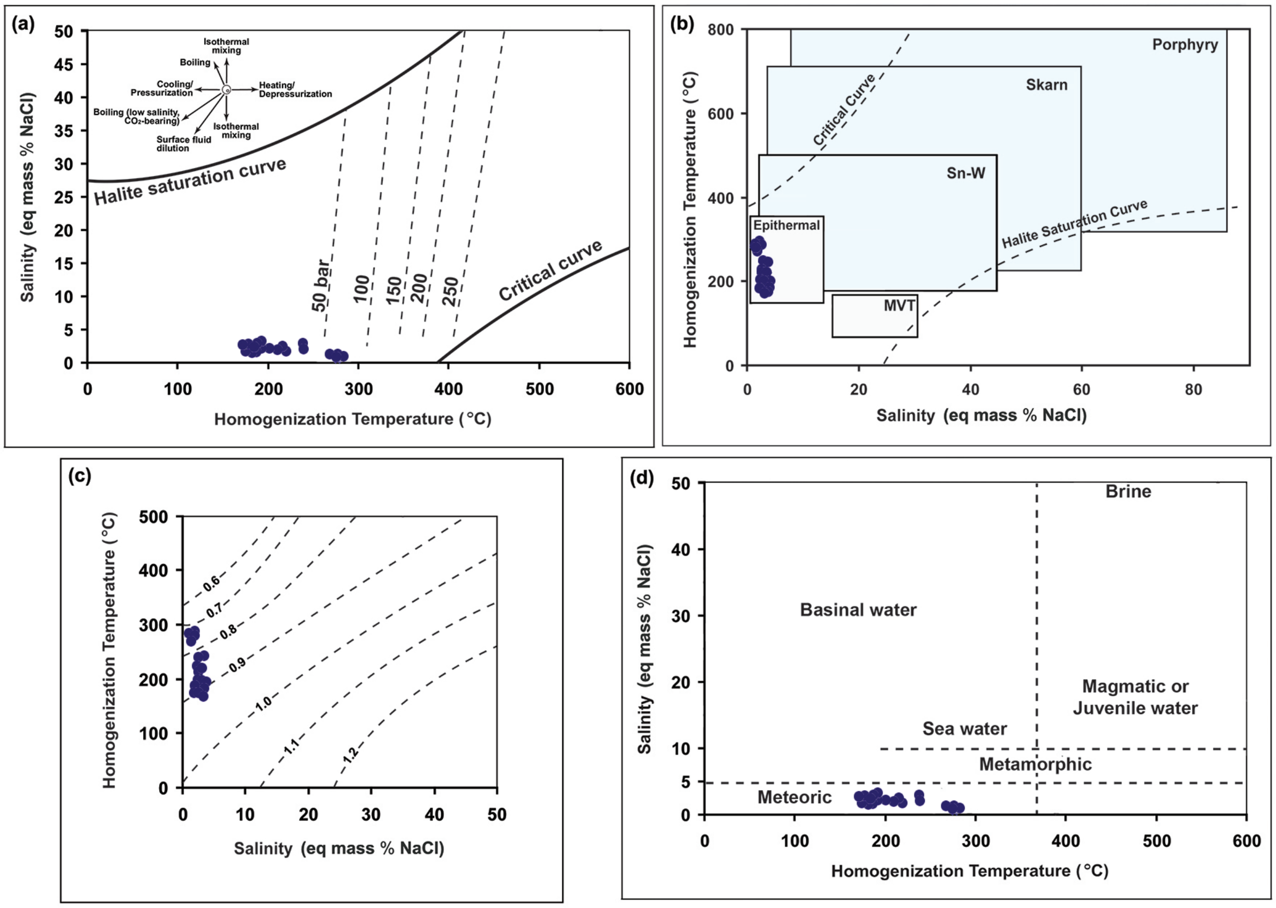

Figure 12. T_h vs. salinity plots illustrating (a) the distribution pattern of the data points relative to the NaCl saturation and critical curves (NaCl saturation and critical curves from Ahmad and Rose, 1980; dashed lines referring to vapor pressures of NaCl solutions at the indicated temperatures and salinities are from Roedder, 1984), (b) the type of mineralization based on the microthermometric data, (c) densities (in gr/cm^3) of the studied fluid inclusions (Wilkinson 2001; contours regressed from data generated by the equation-of-state of Zhang and Frantz (1987), (d) sources of the fluids (Kesler, 2005); the microthermometric data of the Miardan deposit plot within the meteoric water field.

veins/veinlets. In the chondrite normalized distribution patterns of trace and rare earth elements, a distinct negative trend from LREEs to HREEs is seen, which is a typical pattern for many subduction-related young volcanic rocks and suggests the presence of garnet-hornblende as residual phases in the source region of the parental magma, along with restite plagioclase and rutile, conceived from negative anomalies of Sr and Nb-Ta-Ti, respectively, and low to medium degree of partial melting at high pressure.

The T_h and salinity values measured on the 2-phase liquid-rich fluid inclusions range between 176 to 282 °C and 0.65 to 2.6 eq mass % NaCl, respectively, indicating low salinities and moderate to low temperatures of ore-bearing fluids. Most of the salinity data and homogenization temperatures cluster between 1.5 to 2.5 eq mass % NaCl, 170-200 °C and 270-290 °C, respectively, corresponding to epithermal mineralization by fluids of mainly meteoric origin upon cooling.

ACKNOWLEDGEMENTS

This contribution is extracted from the Ph.D. dissertation in the Faculty of Earth Sciences of Urmia University. The authors are also grateful for the financial support provided by the Iran National Science Foundation. The authors would like to express their thanks and appreciation to the anonymous reviewers for their valuable reviews and helpful comments.

REFERENCES

Aghanabati A., 2004. Geology of Iran (in Persian). Geological Survey of Iran, 586 pp.

Aghazadeh M., Hou Z., Badrzadeh Z., Zhou L., 2015. Temporal-spatial distribution and tectonic setting of porphyry copper deposits in Iran: Constraints from zircon U-Pb and molybdenite Re-Os geochronology. Ore Geology Reviews 70, 385-406.

Ahmad S.N. and Rose A.W., 1980. Fluid inclusions in porphyry and skarn ore at Santa Rita, New Mexico. Economic Geology 75, 229-250.

Alavi M., 1994. Tectonics of the Zagros orogenic belt of Iran: New data and interpretations. Tectonophysics 229, 211-238.

Alirezaei S., Einali M., Jones P., Hassanpour S., Arjmandzadeh R. 2016. Mineralogy, geochemistry, and evolution of the Mivehrood skarn and the associated pluton, northwest Iran. International Journal of Earth Sciences 105, 849-868.

Atalou S., Nazafati N., Lotfi M., Aghazadeh M., 2017. Fluid inclusion investigations of the Masjed Daghi copper-gold porphyry-epithermal mineralization, East Azerbaijan Province, NW Iran. Open Journal of Geology 7, 1110-1127.

Bakker R.J., 2012. Package FLUIDS. Part 4: Thermodynamic modeling and purely empirical equations for H_2O-NaCl-KCl solution. Mineralogy and Petrology 105, 1-29.

Package FLUIDS. Part 3: correlations between equations of state, thermodynamics and fluid inclusions.

Barnes H.L., 1979. Geochemistry of hydrothermal ore deposits. John Wiley and Sons, 798 pp.

Barth M.G., Foley S.F., Horn I., 2002. Partial melting Archean subduction zones: Constraints from experimentally determined trace element partition coefficients between eclogitic minerals and tonalitic melts under upper mantle conditions. Precambrian Research 113, 323-340.

Behrouzi A., Amini Fazl A., Amini Azar B., 1997. 1:100000 geologic map of Boastanabad. Geologic Survey of Iran, Tehran, 1 sheet.

Bodnar R.J., 1993. Revised equation and table for determining the freezing point depression of H_2O-NaCl solutions. Geochemical et Cosmochimica Acta 57, 683-684.

Bodnar R.J., 2003. Introduction to fluid inclusions. In: Fluid inclusion-analysis and interpretation (Eds.): I. Samson, A. Anderson, D. Marshall, Mineralogical Association of Canada, Short Course Series 32, 1-9.

Borisenko A.S., 1977. Study of the salt composition of solutions in gas-liquid inclusions in minerals by cryometric method. Soviet Geology and Geophysics 18, 11-19.

Bouzari F. and Clark A.H., 2006. Prograde evolution and geothermal affinities of a major porphyry copper deposit: The Cerro Colorado hypogene protore, I Region, northern Chile. Economic Geology 101, 95-134.

Brenan J.M., Shaw H.F., Ryerson F.J., 1995. Experimental evidence for the origin of lead enrichment in convergent -margin magmas. Nature 378, 54-56.

Calagari A.A., 2003. Fluid inclusion studies in quartz veinlets in the porphyry copper deposit at Sungun, East Azarbaidjan, Iran. Journal of Asian Earth Sciences 23, 179-189.

Calagari A.A., 2004. Geology and fracture-related hypogene hydrothermal alteration and mineralization of porphyry copper deposit at Sungun. Journal of Geological Society of India 64, 595-618.

Chappell B.W. and White A.J.R., 1992. I- and S-type granites in the Lachlan Fold Belt. Transactions of the Royal Society of Edinburgh. Earth Sciences 83, 1-26.

Cooke D.R. and Simmons S.F., 2000. Characteristics and genesis of epithermal gold deposits. Reviews in Economic Geology 13, 221-244.

Floyd P.A. and Winchester J.A., 1975. Magma type and tectonic setting discrimination using immobile elements. Earth and Planetary Science Letters 27, 211-218.

Giese U. and Bau M., 1994. Trace element accessibility in mid-ocean ridge and ocean island basalt: an experimental approach. Mineralogical Magazine 58A, 329-330.

Giese U., Bau M., Dulski P., 1993. Trace element availability during experimental leaching of mid-ocean ridge basalt at 70 °C. Terra Nova 5, 54.

Goldstein R.H. 2003. Petrographic analysis of fluid inclusions. In: Fluid inclusion-analysis and interpretation. (Eds.): I. Samson, A. Anderson, D. Marshall, Mineralogical Association of Canada, Short Course Series 32, 9-54.

Haas J.R., Shock E.L., Sassani D.C., 1993. Prediction of high-temperature stability constants for aqueous complexes of the rare earth elements. Geological Society of America, Annual Meeting in Boston, Mass, Abs. A437.

Hedenquist J.W., Arribas J.A., Gonzalez-Urien E., 2000. Exploration for epithermal gold deposits. Economic Geology 13, 245-277.

Hedenquist J.W., Arribas A.J., Reynolds T.J. 1998. Evolution of an intrusion-centered hydrothermal system: Far Southeast Lepanto porphyry and epithermal Cu-Au deposits, Philippines. Economic Geology 93, 373-404.

Hemley J.J. and Hunt J.P., 1992. Hydrothermal ore-forming processes in the light of studies in rock-buffered systems: II. Some general geologic applications. Economic Geology 87, 23-43.

Jahan Zarjouyan Arasbaran Company, 2018. The 1:1000 geologic map of Miardan. 1 sheet.

Jamali H., Mahmoodabadipour T., Shokohi H., 2017. Geochemical halos of gold and associated elements in Nabijan gold index (SW Kaleibar, NW Iran). Petrology 30,139-156 (in Persian with an English abstract).

Jutteau T. and Maury R., 1997. Geology de la croute oceanique, petrology et dynamique endogens Paris. Mason, 367 pp.

Keppler H., 1996. Constraints from partitioning experiments on the composition of subduction zone fluids. Nature 380, 237-240.

Kesler S.E., 2005. Ore-Forming Fluids. Elements 1, 13-18.

Lindgern W., 1933. Mineral deposits. McGraw-Hill, 930 pp.

Maghsoudi A., Yazdi M., Mehrpartou M., Vosoughi M., Younesi S., 2014. Porphyry Cu-Au mineralization in the Mirkuh Ali Mirza magmatic complex, NW Iran. Journal of Asian Earth Sciences 79, 932-941.

Martin H., 1999. Adakitic magmas: modern analogues of

Archaean granitoids. Lithos 46, 411-429.

Miranvari A.S., Calagari A.A., Ferdowsi R., 2020. Evolution of ore-forming fluids in the Sarilar gold-bearing silicic veins: evidence from fluid inclusions and sulphur stable isotope studies, East Azarbaidjan, NW Iran. Periodico di Mineralogia 89, 265-178.

Montoya J.W. and Hemley J.J., 1975. Activity relations and stabilities in alkali feldspar and mica alteration reactions. Economic Geology 70, 577-594.

Muller D. and Groves D.I., 1997. Potassic igneous rocks and associated gold-copper mineralization. Springer, 238 pp.

Omrani J., Agard P., Whitechurch H., Benoit M., Prouteau G., and Jolivet, L., 2008. Arc-magmatism and subduction history beneath the Zagros Mountain, Iran: a new report of adakites and geodynamic consequences. Lithos 106, 380-398.

Pearce J.A., 1983. Role of sub-continental lithosphere in magma genesis at active continental margins. In: C.J. Hawkesworth, M.L. Nurry (Eds.): Continental basalts and Mantle Xenoliths. Shiva publication (Nantwich), 230-249 pp.

Pe-Piper G., Piper D.J.W., Matarangas D., 2002. Regional implications of geochemistry and style of emplacement of Miocene I-type diorite and granite, Delos, Cyclades, Greece. Lithos 60, 47-66.

Pirajno F., 2009. Hydrothermal processes associated with meteorite impacts. Springer Netherlands, 759 pp.

Rapp R.P., Shimizu N., Miller C.F., 1991. Partial melting of amphibolite/eclogite and the origin of Archean trondhjemites and tonalities. Precambrian Research 51, 1-25.

Rio R., Dupuy C., Dostal J., 1981. Geochemistry of coexisting alkaline and calk-alkaline volcanic rocks from Northern Azarbaijan (NW Iran). Journal of Volcanology and Geothermal Research 11, 253-275.

Robb L., 2005. Introduction to ore forming processes. Blackwell Publishing Company, Malden, MA, 373 pp.

Roedder E., 1984. Fluid Inclusions, Reviews in mineralogy. Mineralogical Society of America, 644 pp.

Rollinson H.R., 1993. Using geochemical data: evaluation, presentation, interpretation. Longman scientific and technical publication, 352 pp.

Seedorff E. and Einaudi M., 2004. Henderson porphyry molybdenum system, Colorado: II. Decoupling of introduction and deposition of metals during geochemical evolution of hydrothermal fluids. Economic Geology 99, 39-72.

Sillitoe R.H., 2000. Gold-rich porphyry deposits: Descriptive and genetic models and their role in exploration and discovery. SEG Reviews 13, 315-345.

Simmonds V., 2013. Geochemistry and petrogenesis of an adakitic quartz-monzonitic porphyry stock and related cross-cutting dike suites, Kighal, northwest Iran. International Geology Reviews 55, 1126-1144.

Simmonds V., 2019. Characteristics and timing of the Cu-Mo mineralization in the Kighal porphyry stock, NW Iran: Implications for the timing of porphyry Cu-related magmatism in Iran and southern Armenia. Ore Geology Reviews 113, 103108.

Simmonds V., Calagari A.A., Kyser K., 2015. Fluid inclusion and stable isotope studies of the Kighal porphyry Cu-Mo prospect, East-Azarbaidjan, NW Iran. Arabian Journal of Geosciences 8, 437-453.

Simmonds V., Calagari A.A., Moayyed M., Jahangiri A., 2011. Investigation on porphyry alteration zones and their geochemical behavior in trace elements and rare earths in Kighal area (North of Varzaghan, East Azerbaijan, Iran) (In Persian). Iranian Journal of Crystallography and Mineralogy 19, 578-565.

Simmonds V. and Moazzen M., 2016. Fluid inclusion studies on Cu-Mo-Au bearing quartz-sulphide veins and veinlets in Qarachilar area, Qaradagh pluton (NW Iran). Periodico di Mineralogia 85, 261-276.

Simmonds V., Moazzen M., Mathur R., 2017. Constraining the timing of porphyry mineralization in NW Iran in relation to Lesser Caucasus and Central Iran; Re-Os age data for Sungun porphyry Cu-Mo deposit. International Geology Review 59, 1561-1574.

Simmonds V., Moazzen M., Selby D., 2019. U-Pb zircon and Re-Os molybdenite age of the Siah Kamar porphyry molybdenum deposit, NW Iran. International Geology Review 61, 1786-1802.

Simmons S.F., Arehart G., Simpson M.P., Mauk J.L., 2000. Origin of massive calcite veins in the Golden Cross, low-sulfidation epithermal Au-Ag deposit, New Zealand. Economic Geology 95, 99-112.

Simmons S.F. and Brown K.L., 2006. Gold in magmatic hydrothermal solutions and the rapid formation of a giant ore deposit. Science 314, 288-291.

Stampfli G.M., 2000. Tethyan ocean, in Bozkhurt, E., Whichester, J.A., and Piper, J.D.A., Eds., Tectonic and magmatism in Turkey and surrounding area. Geological Society of London, Special Publication 173, 1-23.

Sun S.S. and McDonough W.F., 1989. Chemical and isotopic systematics of oceanic basalts: Implications for mantle composition and processes. Geological Society of London, Special Publication 42, 313-345.

Titley S.R. and Beane R.E., 1981. Porphyry copper deposits, Part 1. Geologic settings, petrology and tectonogenesis. Economic Geology 75, 214-235.

Van Middelaar W.T. and Keith W.T., 1990. Mica chemistry as an indicator of oxygen and halogen fugacities in the Can Tung and other W-related granitoids in the North American Cordillera. In: H.J. Stein, J.L. Hannah (Eds.): Ore Bearing Granite System. Geological Society of America Special Paper 246, 205-220.

Wanhainen C., Broman C., Martinsson O., 2003. The Aitik Cu Au-Ag deposit in northern Sweden: A product of high salinity fluids. Mineralium Deposita 38, 715-726.

White A.J.R. and Chappel B.W., 1983. Granitoid types and their distribution in the Lachlan Fold Belt, southeastern Australia. Geological Society of America Special Paper 159, 21-34.

Wilkinson J.J., 2001. Fluid Inclusions in Hydrothermal ore deposits, Elsevier. Lithos 55, 229-227.

Winchester J.A. and Floyd P.A., 1977. Geochemical discrimination of different magma series and their differentiation products using immobile elements. Chemical Geology 20, 245-252.

Wolf M.B. and Wyllie O.J., 1994. Dehydration-melting of amphibolite at 10 kbar: the effects of temperature and time. Contributions to Mineralogy and Petrology 115, 369-383.

Wood S.A., 1990. The aqueous geochemistry of the rare earth elements and yttrium: 2. Theoretical prediction of speciation in hydrothermal solutions to 350 °C at saturation water vapor pressure. Chemical Geology 88, 99-125.

Yang W. and Li Sh., 2008. Geochronology and geochemistry of the Mesozoic volcanic rocks in Liaoning: Implications for lithospheric thinning of the North China Craton. Lithos 102, 88-11.

You C.F., Catillo P.R., Gieskes J.M., Chan L.H., Spivack A.J., 1996. Trace element behavior in hydrothermal experiments: Implications for fluid processes at shallow depth in subduction zones. Earth and Planetary Science Letters 140, 41-52.

Zamora D., 2000. Fusion de la croute oceanique subductee: Approche experimental et geochimique [Ph.D. thesis]. Clermont-Ferrand, University Blaise Pascal, 314 pp.

Zhang Y.G. and Frantz J.D., 1987. Determination of the homogenization temperatures and densities of supercritical in the system NaCl-KCl-$CaCl_2$-H_2O using synthetic fluid inclusions. Chemical Geology 64, 335-350.